VLBA Observations of Mrk 6: Probing the Jet-Lobe Connection

P. Kharb,[1][*] C. P. O'Dea,[2] S. A. Baum,[3] M. J. Hardcastle,[4] D. Dicken,[5]
J. H. Croston,[6] B. Mingo[4,7] and J. Noel-Storr[3]

[1]*Indian Institute of Astrophysics, II Block, Koramangala, Bangalore 560034, India*
[2]*School of Physics and Astronomy, Rochester Institute of Technology, Rochester, NY 14623*
[3]*Chester F. Carlson Center for Imaging Science, Rochester Institute of Technology, Rochester, NY 14623*
[4]*School of Physics, Astronomy and Mathematics, University of Hertfordshire, College Lane, Hatfield AL10 9AB, UK*
[5]*CEA-Saclay, F-91191 Gif-sur-Yvette, France*
[6]*School of Physics and Astronomy, University of Southampton, Southampton, Hampshire SO17 1BJ, UK*
[7]*Department of Physics and Astronomy, University of Leicester, University Road, Leicester LE1 7RH, UK*

ABSTRACT

We present the results of high resolution VLBI observations at 1.6 and 4.9 GHz of the radio-loud Seyfert galaxy, Mrk 6. These observations are able to detect a compact radio core in this galaxy for the first time. The core has an inverted spectral index ($\alpha_{4.9}^{1.6}$=+1.0±0.2) and a brightness temperature of 1×10^8 K. Three distinct radio components which resemble jet elements and/or hot spots, are also detected. The position angles of these elongated jet elements point, not only to a curved jet in Mrk 6, but also towards a connection between the AGN and the kpc-scale radio lobes/bubbles in this galaxy. Firmer constraints on the star formation rate provided by new *Herschel* observations (SFR < 0.8 M$_\odot$ yr^{-1}) make the starburst-wind powered bubble scenario implausible. From plasma speeds obtained via prior *Chandra* X-ray observations, and ram pressure balance arguments for the ISM and radio bubbles, the north-south bubbles are expected to take 7.5×10^6 yr to form, and the east-west bubbles 1.4×10^6 yr. We suggest that the jet axis has changed at least once in Mrk 6 within the last $\approx 10^7$ yr. A comparison of the nuclear radio-loudness of Mrk 6 and a small sample of Seyfert galaxies with a subset of low-luminosity FRI radio galaxies reveals a continuum in radio properties.

Key words: galaxies: Seyfert — galaxies: individual (Mrk 6) — galaxies: jets — techniques: interferometric — radio continuum

1 INTRODUCTION

Markarian 6 is a nearby[1] bulge-dominated lenticular galaxy hosting a Seyfert 1.5 type active galactic nucleus (AGN). Lenticular galaxies are considered to be intermediate between spiral and elliptical galaxies; they have a disk but have either consumed or lost most of their interstellar medium (ISM), so that there is little ongoing star formation activity. At radio frequencies, Mrk 6 exhibits a highly complex morphology: two pairs of self-similar bipolar bubble-like radio structures that are oriented nearly perpendicular to each other are clearly visible (Kharb et al. 2006). While starburst superwinds have been suggested to be mainly responsible for the creation of lobe/bubble-like structures in Seyfert galaxies (e.g., Baum et al. 1993), several pieces of evidence point towards an AGN origin (e.g., Colbert et al. 1996; Elmouttie et al. 1998; Gallimore et al. 2006; Hota & Saikia 2006; Kharb et al. 2006, 2010).

The complex radio morphology of Mrk 6, along with a high degree of polarization ($\sim$ 50% at the edges) and an AGN jet-like spectrum ($\alpha \sim -0.8$; defined throughout as $S_\nu \propto \nu^\alpha$), led Kharb et al. (2006) to suggest that the edge-brightened bubbles were the projections of precessing radio jets. The precessing jets had to shut-off and restart in a nearly perpendicular direction to account for both sets of bubbles. The dominant role played by the AGN in the creation of the radio bubbles was consistent with the low star-formation rate (SFR) of $\leqslant 5.5$ M$_\odot$ yr^{-1} derived from the *Spitzer* Space Telescope data of Buchanan et al. (2006): an SFR of ≈ 33 M$_\odot$ yr^{-1} was required for the bubbles to have been inflated by supernova explosions. New *Herschel* telescope data place even more stringent constraints on the SFR, as discussed ahead.

High-resolution radio observations with the MERLIN[2] interferometer were able to identify individual components in the north-south kpc radio jet (Kukula et al. 1996). As the MERLIN observations were carried out at a single frequency, Kukula et al. (1996) could not identify a flat spectrum radio core in Mrk 6. On the basis of the similar position angles (PAs) of the jet and the brightest regions along the edges of the large north-south lobes, they suggested

---

[*] E-mail:kharb@iiap.res.in
[1] $z = 0.018813$, luminosity distance = 80.7 Mpc

[2] Multi-Element Radio-Linked Interferometer Network

that these bright regions were hot spots created by the north-south jet, where most of the bulk energy of the jets was dissipated; the jet plasma then drifted along the local host galaxy density gradient along the minor axis, forming the rest of the radio lobes. This of course cannot explain the east-west bubbles in this source, because they lie close to the major axis of the galactic bulge (and the galactic disk), where the density gradient is not so pronounced. However, since Kukula et al. did not actually detect the full extent of the east-west bubbles in their observations, this question did not arise. The precessing jet scenario invoked by Kharb et al. (2006) suggested on the other hand, that the jet did not dissipate all its energy in these hot spots but rather continued to advance beyond them to create the 8-shaped radio structures. Furthermore, the precession model indicated that the north-south kpc jet was more closely associated with the east-west bubbles, rather than the north-south bubbles (see Figure 6, Kharb et al. 2006).

In order to re-examine these issues, as well as to search for a flat or inverted spectrum radio core, we observed Mrk 6 with the Very Large Baseline Array (VLBA) at 1.6 and 4.9 GHz. We present here the results from these observations. We also discuss results from two epochs of archival 8.4 GHz VLBA data on Mrk 6. We have used radio bubbles and lobes interchangeably in the text. However, the lobes in Seyfert galaxies differ from those found in powerful Fanaroff-Riley type II radio galaxies (FRII; Fanaroff & Riley 1974) in that they are edge-brightened on all sides (e.g., Mingo et al. 2012) and not just at the leading edges like in FRIIs (e.g., Kharb et al. 2008).

At the distance of Mrk 6, $1''$ corresponds to 377 pc, for $H_0 = 71$ km s^{-1} Mpc^{-1}, $\Omega_{mat} = 0.27$, $\Omega_{vac} = 0.73$.

2   OBSERVATIONS AND DATA REDUCTION

We observed Mrk 6 at 1.65 and 4.98 GHz in a phase-referencing experiment (Beasley & Conway 1995) on 20th October, 2006 (Project ID BK132), with the ten elements of the VLBA (Napier 1994) for a total time of $\approx$12 hours. The total on-source time was $\approx$240 minutes at 1.6 GHz and $\approx$310 minutes at 4.9 GHz. The calibrator DA193 was used as the fringe-finder, while the compact source J0639+7324 with a switching angle of 1.33° and an X, Y positional error of 0.16, 0.22 milliarcsec (mas), respectively, was chosen as the phase reference calibrator[3]. A switching cycle of $\approx$12 mins (calibrator 2 mins, target 10 mins) was adopted at both the frequencies. The calibrator J0621+7605 ($\sim$ 2.65° away and with an X, Y positional uncertainty of 5.81, 2.80 mas) was used as the phase check source. The phase check source is used to get a measure of the decorrelation expected on the target in case of a non-detection.

The observations[4] were made using the standard setup with 128 Mbps recording, a one bit sampling rate, and two 8 MHz intermediate frequencies (IFs) in dual polarization. This yielded a total bandwidth of $(8 \times 2 \times 2 =)$ 32 MHz. We followed the standard VLBA data reduction procedure using the NRAO Astronomical Image Processing System (AIPS, Greisen 2003) as described in Appendix C of the AIPS Cookbook. Delays were corrected using fringe fitting on the fringe finder (with AIPS task FRING). The phase calibrator J0639+7324 was iteratively imaged and self-calibrated on both phase and phase+amplitude using AIPS tasks IMAGR and CALIB. The images were then used as models to determine the amplitude

and phase gains for the antennas. These gains were applied to the target and the final images were made using IMAGR.

The standard self-calibration procedure was not possible for the weak radio components in Mrk 6 at either frequency: the task CALIB had too many failed solutions, irrespective of the weighting and/or uvranges selected. Therefore, phase errors could not be consistently corrected, resulting in the scattering and a net reduction of source flux density. The images displayed in Figures 1 and 2 were created with uniform weighting (with ROBUST=5 in IMAGR). The final rms noise in the image was $\sim$1.5$\times$10^{-4} Jy beam^{-1} at 1.6 GHz and $\sim$6.7$\times$10^{-5} Jy beam^{-1} at 4.9 GHz.

In order to obtain the 1.6$-$4.9 GHz spectral indices, the uv-coverage at both the frequencies was constrained to be identical. The 1.6 and 4.9 GHz images were created using a UVRANGE of 3 - 48 Mλ in task IMAGR. Additionally, a UVTAPER at 32 Mλ was applied to the 4.9 GHz image. The 1.6 GHz image was created using a ROBUST parameter of -0.3. This matching of the shortest and longest baselines resulted in 1.6 and 4.9 GHz images having synthesized beam-sizes close to 5 mas. Therefore, prior to estimating the spectral indices for individual jet components, the 1.6 and 4.9 GHz images were convolved with circular beams of size 5 mas. The spectral indices of components S1 and S2 were finally obtained from integrated flux density values derived from identical-sized regions using the task JMFIT, following the relation, $\alpha = \log(S_{\nu_1}/S_{\nu_2})/\log(\nu_1/\nu_2)$.

We also reduced two epochs of archival 8.36 GHz VLBA data on Mrk 6 from 14th and 24th March, 2011 (Project IDs BC196K, BC196L; PI Jim Condon). J0639+7324 was the phase reference calibrator for Mrk 6. The total on-source time was only $\approx$5 mins. After calibrating in the standard manner and imaging, we failed to detect any emission from Mrk 6 at either epoch. The final rms noise in the images, which was close to the expected thermal noise for this experimental setup, was $\sim 2.0 \times 10^{-4}$ Jy beam^{-1}, and $\sim 3.1 \times 10^{-4}$ Jy beam^{-1}, for the March 14 and March 24 data, respectively[5].

The new *Herschel* data discussed ahead in Section 4, were obtained from the *Herschel* Science Archive from the program OT1_rmusholtz_1. Both the PACS and SPIRE data were processed with the *Herschel* HIPE analysis software (version 10.0.0). The PACS data were acquired in March 2012 in the standard photometry mode at wavelength filters 70 and 100μm and were reduced with default scripts for extended sources. The SPIRE data were taken in September 2011 at 250, 350 and 500μm in the small scan mode and were reduced in HIPE using scripts developed for optimum processing at the Institut d′Astophysique Spatiale. Fluxes were measured using the HIPE aperture photometry tool and the uncertainty reported is the calibration uncertainty combined in quadrature with the variation in the background measured, at random, with identical apertures.

3   RESULTS

We detected three distinct radio components at 1.6 GHz. These are identified as N, S1 and S2 in Figure 1. Components S2, S1, and N correspond to components 2, 4 and 6 of Figure 1 of Kukula et al. (1996), respectively. All components appear resolved: the position angles of their extensions are indicated in the left panel of Figure 1. The centre of the optical host galaxy of Mrk 6 (indicated as a cross

---

in Figure 1) is at RA 06h 52m 12.251s, Dec +74° 25′ 37.46″, with an uncertainty ellipse of 0.36″ × 0.30″ at PA 90° (Li & Jin 1996). At 4.9 GHz, we detected components S1 and S2 only (see Figure 2).

We also detected with a significance of 6σ a compact component at 4.9 GHz which we propose is the radio core of Mrk 6, at a position of RA 06h 52m 12.32333±0.00004s, Dec 74° 25′ 37.2376±0.0002″ (see Figure 3). The identification of this compact component as the radio core is validated by its spectral index and brightness temperature values, as discussed below. We note that the systematic errors in the component positions are much larger than the errors quoted here from JMFIT, and are typically of the order of $0.1-0.2$ mas (e.g., Ma et al. 1998). The peak intensity and total flux density of the core is 0.4 mJy beam^{-1} and 0.5 mJy, respectively. The beam-deconvolved size of the core is 1.86 mas × 0.46 mas, (=0.7 pc × 0.2 pc; however see more discussion on this below). The core minor axis of 0.2 pc corresponds to 10^4 times the Schwarzschild radius (R_s) in Mrk 6, for a black hole mass of $\sim 2 \times 10^8 M_\odot$ (Doroshenko et al. 2012). While compact jet-dominated cores are expected to have sizes of $\sim 10^3 - 10^4 \, R_s$ (similar to what we find in Mrk 6), and advection-dominated accretion flows (ADAF; Mahadevan 1997) should have core sizes of $\sim$10s of R_s (Ulvestad 2003; Anderson & Ulvestad 2005), the highest achievable angular resolution on Earth restricts one from truly differentiating between a jet-dominated and an ADAF-dominated core.

We note that the core detected here is distinct from component 5 of Figure 1 of Kukula et al. (1996), as it is only 58 mas (=22 pc) from component S1, while component 5 is about 200 mas (=75 pc) away from component 2 (i.e., component S1 in present paper). Therefore, VLBI observations were crucial in the identification of the radio core in this galaxy. Component 5 of Kukula et al., which was not detected in the present data, could be counterjet emission, as the real core lies between component 5 and component 4 (S1 here). This counterjet emission must be more diffuse than the jet emission (S1), so that VLBI observations fail to detect it.

The mean spectral index of component S1 is -0.3 ± 0.2, and component S2 is -0.6 ± 0.2. The relatively flat spectral index of component S1 could be suggestive of the jet segments being currently powered by the AGN (i.e., with relativistic particles being currently injected into it), or to particle acceleration in a shock. As the core was not clearly detected either at 1.6 GHz or 8.4 GHz, we use two times the rms noise values in the region of the expected core as an upper limit to the core flux density at 1.6 GHz and 8.4 GHz. For an integrated core flux density at 4.9 GHz of $\sim$0.41 mJy, we estimate that the $1.6-4.9$ GHz and $4.9-8.4$ GHz spectral indices are $\geqslant 0.4$ and $\leqslant -0.05$, respectively. Two times the rms noise was chosen as a conservative upper limit because of the dependence of noise on the number of CLEAN iterations specified in IMAGR. These spectral index limits are in general agreement with the flat or inverted radio spectra routinely observed in Seyferts cores on different spatial scales (e.g., Nagar et al. 2000; Ulvestad & Ho 2001).

We estimated the brightness temperature of the radio components using the relation, $T_B = 1.8 \times 10^9 (1 + z) \left(\frac{S_\nu}{1\,mJy}\right) \left(\frac{\nu}{1\,GHz}\right)^{-2} \left(\frac{\theta_1 \theta_2}{mas^2}\right)^{-1} K$, where θ_1, θ_2 are the major, minor axes of the best-fitting elliptical Gaussian for a resolved radio component (Ulvestad, Antonucci & Barvainis 2005). Component sizes were derived using the Gaussian-fitting task JMFIT in AIPS. For the unresolved core, we multiplied ($\theta_1 \theta_2$) by a factor of 1/2, under the assumption that half the beamsize was the upper limit to the size of the unresolved component (see Ulvestad, Antonucci & Barvainis 2005). The brightness tempera-

ture of the radio core is 1×10^8 K, and is consistent with non-thermal synchrotron emission. The brightness temperature is a lower limit because the assumed core size is an upper limit. T_B is typically around $\sim 10^7$ K for components S1, S2 and N (see Table 1), and is similar to the brightness temperatures observed in other Seyfert nuclei (e.g., Kukula et al. 1999; Middelberg et al. 2004; Orienti & Prieto 2010). The high brightness temperatures provide support for a non-thermal origin of the radio emission.

Component S1 resembles a jet element at a PA of $\sim 150°$, while components S2 and N are arc-like or hot spot-like features that are stretched in a direction roughly perpendicular to the PA of the jet feature in component S1. The PA of a line joining the core and S1 is $\approx 145°$, close to the elongation of component S1 itself. The bright edges and the hot spots along the edges of the kiloparsec radio lobes, resemble the projection of a highly curved radio jet.

We estimated the magnetic field strength for a cylindrical jet geometry, under the minimum-energy assumption for relativistic particles and magnetic fields (Burbidge 1959; Miley 1980). Images convolved with 5 mas beams were used to obtain the flux densities and sizes of the radio components (with JMFIT). The minimum-energy magnetic field strength was obtained by numerically minimising the sum of electron and magnetic field energy density, assuming powerlaw electron energy spectra with energy indices corresponding to $\alpha = -0.3$ for component S1 and $\alpha = -0.6$ for component S2. We assumed that for all the components $\gamma_{\min} = 10$, $\gamma_{\max} = 10^5$ (the results depend only weakly on these assumptions). For a true minimum energy density, we assumed no additional contribution to the energy density from protons and a filling factor of unity. The minimization was carried out using the code of Hardcastle, Birkinshaw & Worrall (1998). The minimum B-field strength turns out to be of the order of a milliG, while the minimum pressure is a few times 10^{-8} dyne cm^{-2} (see Table 1).

As the radio core is detected at 4.9 GHz, but not at 1.6 GHz or 8.4 GHz, we can assume the turnover frequency (ν_m) of the core's powerlaw emission to lie between 1.6 and 8.4 GHz. Then an estimate of the magnetic field strength (in G) can be made, assuming that the frequency turnover is due to synchrotron self-absorption rather than free-free absorption, following the relation from Kellermann & Pauliny-Toth (1981): $B = \frac{\nu_m^5}{f(\gamma)^5 S_m^2 \theta^{-4} (1+z)}$, where $f(\gamma)$ is a weakly dependent function of the electron energy index γ, and is $\sim$8 for γ=2 (*i.e.*, for $\alpha = \frac{1-\gamma}{2} = -0.5$); S_m is the maximum synchrotron flux density in Jy, ν_m is in GHz, and θ is the angular size in milliarcseconds. As the derived magnetic field strength is a very strongly dependent function of ν_m and θ, and the Gaussian-fitting task JMFIT typically fails to constrain the minor axis of the deconvolved core, there can be a large uncertainty in the derived magnetic field strength. For an assumed ν_m of 5 GHz, the B field can vary from 1.5×10^5 G to 2 mG, for θ varying from [1.86 mas × 0.46 mas, or 0.7 pc × 0.2 pc] to [1.86 mas × 0.005 mas, or 0.7 pc × 0.002 pc]. Note that the former θ is derived from one set of "nominal" major and minor axes values derived with JMFIT, the minor axis in the latter θ has been chosen to be arbitrarily small (since JMFIT does not typically constrain it but only indicates that it is much smaller than the beam-size of the image = 2 mas × 2 mas). This latter θ value was in fact chosen to get a B field estimate that was comparable to the minimum-energy magnetic field value derived in Table 1. However, if the turnover frequency was closer to 1.6 GHz, then the unconstrained minor axis of the deconvolved core could be 4 times larger and the B field could still be close to equipartition (~ 2 mG). All in all, our data are not precise enough to get a robust magnetic field estimate, and

Table 1. Observed and Derived Parameters

Comp	Flux mJy	Length mas	Width mas	B_{min} milliG	P_{min} dyn cm^{-2}	t_{life} yr	T_B K
S1_1.6	2.9	12.1	4.7	1.2	4.6×10^{-8}	8772	3.4×10^7
S2_1.6	3.8	12.6	10.2	1.0	2.9×10^{-8}	11531	2.0×10^7
N_1.6	5.8	31.5	19.7	0.6	1.0×10^{-8}	1172	6.2×10^6
S1_4.9	2.3	7.0	5.7	1.7	9.6×10^{-8}	5202	4.4×10^6
S2_4.9	2.0	7.9	6.9	1.4	5.9×10^{-8}	6961	2.7×10^6

Column 1: Component name: S1_1.6 and S1_4.9 refer to component S1 at 1.6 and 4.9 GHz, respectively, and so on. Columns 2, 3 and 4: The integrated flux density, length and width of the resolved components were obtained from the elliptical Gaussian-fitting task JMFIT in AIPS. These estimates were derived from 1.6 and 4.9 GHz images convolved with circular beams of size 5 mas. As component N was resolved out in the 5 mas image, a 6 mas image was used instead for this component. Columns 5 and 6: Minimum energy magnetic field strength and pressure, respectively. The spectral index for component N was assumed to be the same as component S2 $=-0.6$. Column 7: Lifetime of electrons undergoing synchrotron radiative and inverse Compton losses on CMB photons for a break frequency of 4.9 GHz. Column 8: Brightness temperature at 1.6 and 4.9 GHz, respectively, for the resolved components.

we cannot say with certainty if the B field is close (or not) to the equipartition value. Bontempi et al. (2012) have suggested that the excessively large magnetic field estimates derived in their VLBI observations of Seyfert cores are consistent with thermal, rather than synchrotron emission.

The lifetime of electrons in the jet components undergoing both synchrotron radiative and inverse Compton losses on CMB photons, was estimated using the relation $t_e \simeq 2.6 \times 10^4 \frac{B^{1/2}}{B^2+B_r^2} \frac{1}{[(1+z)\nu_b]^{1/2}}$ years (van der Laan & Perola 1969), where B was assumed to be the equipartition magnetic field B_{min}, and the break frequency ν_b was assumed to be 4.9 GHz. The magnetic field equivalent to the radiation, which was assumed to be predominantly CMB photons, B_r, was estimated using the relation, $B_r \simeq 4 \times 10^{-6}(1 + z)^2$ Gauss, where z is the source redshift. The electron lifetimes lie between $5000-11,000$ years. These lifetimes are about 30 percent shorter than if only synchrotron losses were prevalent. However, it has been pointed out that stellar photon density may be much higher than the CMB photon densities in nearby elliptical galaxies (Stawarz, Sikora & Ostrowski 2003; Hardcastle & Croston 2011). As this may also hold for bulge-dominated S0 type galaxies which host Seyfert nuclei, we can expect that the inverse Compton losses will be higher than estimated here, and this will reduce the electron lifetimes further. An additional caveat is that since self-calibration could not be carried out while imaging the source, a significant amount of flux density could be missing from the radio components. A higher radio flux density will imply higher B_{min} values and lower electron radiative lifetimes.

4 DISCUSSION

In Kharb et al. (2006), we had estimated that the star formation rate derived from *Spitzer* observations was far below that required to inflate the radio bubbles. Additional evidence for a comparatively low SFR comes from new *Herschel* data which we obtained from the *Herschel* archive and reduced using the *Herschel* analysis software HIPE (see Section 2 for details). We present in Figure 4 the broadband SED of Mrk 6 with new *Herschel* infrared data using the PACS and SPIRE instruments (Poglitsch et al. 2010; Griffin et al. 2010). No previous data existed in this part of the spectrum and this figure clearly shows the importance of the new *Herschel* data for tracing the infrared peak of the SED, which originates in AGN and/or star formation heated dust emitting in the infrared. These *Herschel* data have the advantage over previous *Spitzer* measure-

ments in that the star formation is thought to be the dominant heating mechanism of the dust that produces emission at these longer wavelength in the far-infrared. At *Spitzer* wavelengths (i.e. 24μm) a considerable contribution to the 24μm luminosity may be expected from the AGN instead. Therefore, the SPIRE 250μm band can give a better estimate of the SFR than was previously possible with *Spitzer*. Calculating the luminosity at 250μm (L250μm) for Mrk 6 and using the empirical relation derived by Hardcastle et al. (2013) for L250μm versus SFR, measured from optical spectral modelling, we find a low SFR of 0.8 M$_\odot$ yr^{-1}. This SFR is also an upper limit because the 250μm flux can originate both from cool dust heated by the old stellar population as well as from young star forming regions. It is also noteworthy that Mrk 6 has no strong evidence for star formation tracing polycyclic aromatic hydrocarbon (PAH) features in contrast to the majority of Seyfert galaxies (Gallimore et al. 2010). Therefore, for the remaining discussion we have assumed that AGN jets are primarily responsible for the creation of the radio bubbles. We discuss the morphology of the radio jets, their connection to the kpc-scale bubbles, and the bubble ages in the following sections. Finally we discuss the radio-loudness of Mrk 6 and other Seyfert galaxies and compare them to those of low luminosity FRI radio galaxies.

4.1 Changes in Jet Direction: Interaction with the Medium

Kinney et al. (2000) used the distribution of radio jet orientation in Seyfert galaxies to show that the accretion disks are commonly misaligned with the host galaxy disk. There are several reasons why this might be the case, including misaligned inflow of gas from a minor merger. The misaligned gas inflow will change the accretion disk axis, and the blackhole will re-align with the disk via Lense-Thirring precession (Bardeen & Petterson 1975; Rees 1978). Minor mergers could be responsible for the creation of randomly-oriented short-lived accretion disks in Seyfert galaxies, that could in turn lead to jet precession (e.g., Volonteri, Sikora & Lasota 2007). Another mechanism for a change in the jet axis would be a merger with another black hole (e.g., Merritt & Ekers 2002). For the brightest cluster galaxy of RBS797, which exhibits orthogonal radio outflows, a jet flip due to the presence of a binary black hole has been suggested by Gitti et al. (2013). ISM rotation and ram pressure bending have also been invoked to explain the curved radio jets in some Seyfert galaxies (e.g., Wilson & Ulvestad 1982). While jet flips alone may arise from a minor merger event, both jet precession and jet flips, as discussed for Mrk 6 ahead, can naturally occur due to the presence of binary black holes.

The archival *Hubble Space Telescope (HST)* Advanced Camera for Surveys (ACS) F330W image[6] of Mrk 6 shows the presence of a tail-like feature towards the north-west, which could be a signature of past merger activity in Mrk 6. The emission line images of [OIII] and [OII] from the Faint Object Camera (FOC) aboard the *HST* show that there is dense emission line gas in the direction of the nucleus in Mrk 6, which could provide the clouds which merge with the accretion disk. The emission line images show a clear correspondence with the southern part of the MERLIN radio jet (see Capetti et al. 1995). Capetti et al. however used a weak radio component in between S1 and S2 as the radio core to align their emission-line image. When the detected radio core is properly aligned, we find that the radio component S2 lies at the outer edge of the bend observed in the S-shaped emission line region (see Figure 5). This close correspondence could be indicative of interaction between the radio ejecta and the surrounding medium (e.g., Capetti et al. 1995). *Chandra* and *XMM-Newton* observations of Mrk 6 have shown that the X-ray emitting gas has a complex structure (Schurch, Griffiths & Warwick 2006; Mingo et al. 2011). This is also consistent with a jet that is changing its direction of propagation, interacting with the surrounding ISM.

4.2 A Curved Jet due to Precession ?

We first examine the precession model to explain the S-shaped jets in Mrk 6. The precession model is in keeping with the basic idea proposed by Kukula et al. (1996), namely, that the north-south jets are producing the hot spots along the edges of the kpc-scale north-south bubbles. We note that Kelvin-Helmholtz instabilities that arise in relativistic jets due to some perturbation at the jet nozzles could also produce helical twisting patterns in jets (e.g., Hardee 1987). At the end of the section, we examine an alternate model proposed by Mingo et al. (2011) to explain the Mrk 6 lobes.

Following the relations of Hjellming & Johnston (1981), we created a precessing jet model, and superimposed it on the VLBA and VLA radio images of Mrk 6 (see Figure 6). The 20cm VLA image is reproduced from Kharb et al. (2006). The new core position was chosen as the origin for this jet model. The projected precessing jet model matches the radio features well. The best fit model parameters for a clockwise rotating jet are: jet speed = $0.13c$ ($\sim 3.9 \times 10^4$ km s^{-1}), jet PA = $-87°$, jet inclination = $144°$, jet precession cone half-opening angle = $37°$, and jet angular velocity = 1.5×10^{-6} rad yr^{-1}. It is important to note that the above set of parameters is not unique, and another combination of the parameter set could also result in a good fit to the apparent radio morphology. This is also demonstrated by the fact that the best fit parameters presented here differ from those derived in Kharb et al. (2006), although different spatial scales were examined in the two cases. One therefore needs independent measurements of as many parameters as possible (e.g., jet speed, jet inclination), to realistically constrain the precession model. However, it is important to note that precessing jets have independently been inferred in Seyfert galaxies, through core flux and PA variability studies, carried out by multi-epoch VLBI obervations (e.g., III Zw 2 & M 82; Brunthaler et al. 2005; Martí-Vidal et al. 2011).

For the best fit jet speed and inclination obtained here, a jet-to-counterjet intensity ratio ($\equiv [1 + \beta \cos \theta / 1 - \beta \cos \theta]^p$) of 0.6 is expected for a jet structural parameter, p of 2.3, and 0.5 for a

p of 3.3 ($p = 2 - \alpha$, or $3 - \alpha$ for a continuous or "blobby" jet, respectively; Urry & Padovani 1995). It is interesting though that no jet or counterjet emission is detected to within 22 parsec of the core. While such a gap is traditionally considered to be a signature of relativistic deboosting in fast jets that are lying close to the plane of the sky, it is difficult to assume the same for Seyfert galaxies, since Seyfert jets are expected to be only mildly relativistic (e.g., Bicknell et al. 1998; Middelberg et al. 2004).

The way it is depicted in Figure 6, the jet has been "on" for 1.4×10^5 yr. This time constraint follows from the basic idea proposed by Kukula et al. (1996) that the north-south jet gets disrupted after forming hot spots along the edges of the north-south lobes. Therefore, 1.4×10^5 yr was the time the jet must have been "on" in the precession model, in order for it to be disrupted around the position of the bright edges or hot spots of the north-south bubbles (as determined visually from Figure 6). From this best fit model, it is apparent that component N is not a part of the jet that connects the parsec scale emission to the kpc-scale north-south bubbles, but is rather a part of the east-west bubbles. This is also seen by the PA of its extension in the left panel in Figure 1. The east-west extensions in Figure 3 of Kukula et al. (1996), which are clearly part of the east-west bubbles, also have the same PA. The fact that this radio component has the steepest spectra (actually only a lower limit) of the three detected components, could be consistent with it arising from a different AGN activity episode, compared to components S1 and S2. The steep spectrum of component N could suggest electron radiative decay in older radio emission. However, this is inadequate evidence by itself, since the spectrum of component S2 is also steep. While the MERLIN observations of Kukula et al., were unable to resolve components S1 and S2 for the purpose of estimating the 1.6−4.9 GHz spectral indices, they derived an average $\alpha = -0.8$ for that part of the jet. Their component 6 (component N here) was easily resolved and had a somewhat steeper spectral index of -0.9.

Apart from the redundancies present in the best-fitting model, another caveat of the precession model, as presented here, is that it suggests that the jet is currently powering the larger north-south lobes, rather than the smaller but brighter east-west lobes. While the extended narrow line region, which is likely being photoionized and/or shock-ionized by the AGN, does lie along the north-south direction, consistent with this being the current jet direction; the size and surface brightness of the east-west lobes are suggestive of them being the ones that are newly formed.

Another model, suggested by Mingo et al. (2011), proposes that the bubbles are edge-brightened lobes created by the AGN that are expanding into the ISM. This scenario also requires a flip in the AGN jet axis. This model is consistent with the X-ray observations which detect shocked gas (albeit only in small regions) ahead of the radio lobes. A drawback of this model is that it cannot explain why the upper edge of the northern lobe and the lower edge of the southern bubble is relatively brighter than the opposite edge. This effect is much more pronounced in the east-west bubbles where the lower edge of the east bubble and upper edge of the west bubble is brighter. If we assume that the ram pressure of the lobe against a counter-clockwise rotating ISM is responsible for the selective edge brightening in the north-south lobes, then the ISM rotation would need to be clockwise to explain the bright opposite edges in the east-west lobes. This could be a big drawback for the edge-brightened lobe model. Selective edge brightening can more easily be explained as directional, albeit curved, AGN outflows.

---

[6] Program ID 9379, PI - Henrique Schmitt, http://archive.stsci.edu/cgi-bin/mastpreview?mission=hst&dataid=J8EK17011

4.3 Constraints on Bubble Ages from Radio and X-ray Observations

Mingo et al. (2011) estimated that the total work available from the plasma filling the north-south lobes was $\approx 4 \times 10^{56}$ erg. For the AGN jet with a total radio luminosity of say, $\approx 10^{40}$ erg s^{-1} (Kharb et al. 2006, Table 3), and kinetic luminosity of 10^{42} erg s^{-1} (assuming an efficiency of conversion of 1 percent; O'Dea 1985; Bîrzan et al. 2007), the jet would require 1.3×10^7 years to power the north-south lobes. This is about 90 times longer than the time the jet was "on" in the precessing jet model. The two timescales would be comparable if the conversion efficiency was lower than 0.1 percent.

Based on the Mach number M of the shock producing the X-ray emission at the outer edges of the north-south bubbles in Mrk 6 ($M = 3.9$), Mingo et al. (2011) estimated that the speed of the plasma in the bubbles was around 1030^{+75}_{-100} km s^{-1}. From the *Chandra* observations, they also estimated that the electron density of the ISM outside the bubbles varied from 8 - 40×10^{-4} cm^{-3}. This implies that the ISM gas mass density (obtained by multiplying the ISM electron density with the mass of the hydrogen atom $= 1.67 \times 10^{-24}$ g) varies from $1.3 - 6.7 \times 10^{-27}$ g cm^{-3}. If the minimum pressure of the north bubble varies from 1.2×10^{-12} dyne cm^{-2} to 6.2×10^{-11} dyne cm^{-2} for a filling factor of 1.0 and 10^{-3}, respectively (see Table 3, Kharb et al. 2006), then the velocity of the lobe plasma can be estimated assuming that the lobe is in ram pressure balance with the surrounding ISM. Using the relation $P_{min} = \rho_{ISM} v_{lobe}^2$ and the ISM gas density from above, we find that v_{lobe} varies between ~ 130 to 960 km s^{-1} for a gas density of 6.7×10^{-27} g cm^{-3}, and between ~ 300 to 2150 km s^{-1} for a gas density of 1.3×10^{-27} g cm^{-3}. Assuming that the plasma velocity inside the lobes was around 1000 km s^{-1}, the north bubble of extent 7.7 kpc would take 7.5×10^6 years to form, while the east bubble of extent 1.4 kpc would take 1.4×10^6 yr to form for the same plasma speed. However, as *Chandra* could not clearly resolve the X-ray emission from the east-west bubbles, the plasma speed and therefore the age is uncertain for the east-west structure. It is only clear that the jet axis in Mrk 6 has changed at least once within the last $\approx 10^7$ yr.

4.4 The Radio Loudness of Seyferts

Seyfert galaxies have been historically identified as radio-quiet AGN. Kellermann et al. (1989) defined the radio-loudness parameter, R, of an AGN to be the ratio of its radio flux density at 5 GHz to its B-band optical flux density at 4400 Å, with the radio-quiet/radio-loud AGN division set at $R \sim 10$. As Seyferts reside in spiral or S0-type host galaxies, and radio-loud AGN are typically hosted by elliptical galaxies, explanations for the "lack" of large-scale radio emission in Seyferts, have focused on differences in their central engines, which are in turn dependent on their host galaxy types. For instance, differences in black hole masses and spins, both of which are different in spiral and elliptical galaxies, have been suggested to explain the differences in the radio-loudness properties (e.g., Sikora, Stawarz & Lasota 2007). It is in this context that it is interesting to note that Mrk 6 has an R value of ≈ 23, making it a radio-loud Seyfert galaxy (the total 5 GHz flux density as measured by the single dish Green Bank Telescope for Mrk 6 is 115 ± 9 mJy (Gregory & Condon 1991), while the B-band appar-

ent magnitude is 14.88 ± 0.16 mag (NED)[7]). The mere existence of radio-loud Seyferts can provide strong constraints on the jet production mechanisms in AGN.

The inherent assumption in the estimation of R above, is that the B-band luminosity is dominated by the AGN light, which is unlikely to be true for Seyfert galaxies. Ho & Peng (2001) extracted the optical nuclear luminosities for a large number of Seyfert galaxies through a proper modelling of their galactic bulge emission in *HST* images. Remarkably, after taking into account their optical nuclear luminosities, Ho & Peng found that a majority of Seyfert 1 galaxies were radio-loud. A similar conclusion was reached by Terashima & Wilson (2003) on the basis of the radio to X-ray flux density ratio for a sample of low luminosity AGN including Seyferts. We present in the Appendix a comparison of the radio-loudness parameters of Seyfert (1 and 2) galaxies belonging to the Extended $12\mu m$ sample of Rush, Malkan & Spinoglio (1993), along with a sample of UGC FRI radio galaxies, having taken into account their optical nuclear luminosities. We estimate that, even without acknowledging the AGN-only contribution to the optical luminosity, ≈ 11 percent of Seyfert galaxies (both type 1s and 2s) from the Extended $12\mu m$ complete sample of Rush, Malkan & Spinoglio (1993) can be classified as radio-loud following the Kellermann et al. definition. This fraction increases to $\geqslant 70$ percent, when the optical nuclear luminosities are considered (see Table A1).

We have plotted in Figure 7 the radio-loudness parameter values for these Seyfert galaxies, along with those of 21 UGC FRI radio galaxies (Verdoes Kleijn et al. 1999; Kharb et al. 2012b). There is an overlap between the R values of this subset of Seyferts and those of low luminosity FRI radio galaxies. Balmaverde & Capetti (2006) and Kharb et al. (2012a) also found a continuum of properties in the host galaxy surface brightness profiles as observed by the *HST*, which reflects on the galaxies' nuclear structures, for a small sample of Seyfert and FRI radio galaxies. Although on average Seyfert galaxies have less massive blackholes than FRI radio galaxies, there is an overlap in the blackhole mass ranges for the two classes: $\sim 10^7 - 10^8$ M$_\odot$ for Seyferts (Wandel, Peterson & Malkan 1999), and $\sim 10^8 - 10^9$ M$_\odot$ for FRI radio galaxies (Woo & Urry 2002).

There is also a continuum in the radio morphological properties of FRI galaxies and radio-loud Seyfert galaxies, although more sensitive observations are required to map the diffuse lobe emission in the latter. In the absence of sensitive radio observations of Seyfert galaxies, we can restrict our comparison to individual sources, which prevents us from claiming a statistically significant overlap in radio morphology between Seyfert galaxies and low luminosity FRIs. The radio structure in the Seyfert galaxy, Circinus, with hot spot like features immersed in bubble-like lobes (see Mingo et al. 2012), resembles the hot spot-lobe structure observed in the FRI radio galaxy, Hercules A (Gizani & Leahy 2003; O'Dea et al. 2013). While the radio bubbles of Mrk 6 and other Seyfert galaxies (e.g., NGC 6764) are typically a few kpc to ~ 10 kpc across, and are confined to the bulge of the host galaxy, bipolar bubbles of extent >100 kpc have been observed in the radio galaxy, NGC 1167 (Shulevski et al. 2012). Interestingly, the FRI radio galaxy with the lowest nuclear radio-loudness parameter in the sample under study, UGC 03695 (R=3775), has a radio structure very similar to that seen in Seyfert galaxies (see Figure 8). These data are from our VLA program AB920 (J. Noel-Storr et al.,

---

[7] NASA/IPAC Extragalactic Database

in preparation). The lower frequency image (1.4 GHz) shows the bipolar bubble-like lobes, while the higher frequency image (4.9 GHz) shows a jet-like (i.e., elongated) structure pointing toward the western edge of the north lobe. This not only suggests a close connection between the jet-like structure and the bubble-like lobes, but also the presence of a misaligned jet. Small-scale jets that are misaligned with the radio lobes are a common characteristic of Seyfert galaxies.

S0 galaxies resemble elliptical galaxies in terms of their bulge properties, but additionally have low density gas and dust-rich disks in their centres. It is then plausible that the radio jets in Seyfert galaxies, which likely arise from the inner accretion disks (e.g., Nixon & King 2013) are affected by the presence of these kpc-scale dusty disks, and precess. Any kind of warp that develops in the disk close to the jet launching sites, as a result of misalignment with the large scale galactic disks, may affect the jets so that they are no longer straight. Moreover, the distance from the cores where the jets "flare", or decollimate and widen, like in FRI radio galaxies (e.g., Laing & Bridle 2002, the flaring distance is typically 1 kpc in FRIs), could be shorter for Seyfert galaxies. Subsonic jets moving in a confined medium where the density varies more slowly that $1/R^2$, where R is the distance from the galaxy centre, could produce bubble-like radio structures (Falle 1991). Therefore, we propose that a combination of an early-flaring, misaligned jet in a confined medium could produce Mrk 6-like radio lobes, and similar lobes observed in other Seyfert galaxies.

5 SUMMARY

We have presented here high resolution VLBA observations at 1.6 and 4.9 GHz of the ~1 kpc radio jet in the radio-loud Seyfert galaxy, Mrk 6.

(i) We detect 3 distinct radio components, N, S1, S2, at 1.6 GHz, but only components S1 and S2 at 4.9 GHz. However, the 4.9 GHz observations show the presence of an inverted spectrum radio core ($\alpha_{4.9}^{1.6}$=+1.0±0.2), with a brightness temperature of $\approx 10^8$ K, indicating that it is the base of a relativistic synchrotron jet. This core had not been detected in prior radio observations: VLBI proved to be crucial in the identification of this core.

(ii) The mean spectral index $\alpha_{4.9}^{1.6}$ of component S1 is -0.3 ± 0.2 and S2 is -0.6 ± 0.2. The relatively flatter spectral index of component S1 is consistent with it being currently powered by the AGN, or to particle acceleration in a shock.

(iii) Additional 8.4 GHz archival VLBA data on Mrk 6 failed to reveal any radio emission. We estimate that the $4.9-8.4$ GHz spectral index of the core is steeper than -0.05.

(iv) All the detected components, apart from the core, are resolved and elongated, such that they appear to be either jet segments or hot spots, where the jet impacts the surrounding ISM. The position angles of these components also indicate a connection to one edge of the north-south kpc-scale radio lobes, although no emission is detected continuously to clearly show this connection. More sensitive observations are required to detect the inter-jet-segment emission.

(v) New *Herschel* 250μm observations provide an upper limit to the star formation rate in Mrk 6 of 0.8 M$_\odot$ yr^{-1}. This estimate is nearly 40 times lower than the SFR required to inflate the radio bubbles ($\approx$33 M$_\odot$ yr^{-1}; Kharb et al. 2006). The AGN jet is therefore primarily responsible for the creation of the radio bubbles in Mrk 6.

(vi) With the estimated total jet radio luminosity of $\approx 10^{40}$ erg s^{-1}, the jet will take 1.3×10^7 yr to power the north-south bubbles with a total energy of $\approx 10^{56}$ erg (Mingo et al. 2011). From plasma speeds of the order of 1000 km s^{-1} obtained through the X-ray observations of Mingo et al. (2011), and ram pressure balance arguments for the ISM and the bubbles, the north-south bubbles are expected to take 7.5×10^6 yr to form, and the east-west bubbles 1.4×10^6 yr. We suggest that the jet axis has changed at least once in Mrk 6 within the last $\approx 10^7$ yr. This is consistent with the signatures of a minor merger that this galaxy seems to have undergone, as observed in its *HST* image.

(vii) Although from these observations alone, it is difficult to identify the primary mechanism for the curved radio jet in Mrk 6, jet precession can explain the morphology from parsec to kiloparsec scales. While jet flips alone may arise from a minor merger event, both jet precession and jet flips can naturally occur in the presence of binary black holes.

(viii) Both the *HST* imaging which shows a close alignment between the emission-line gas and the radio jet, and the *Chandra* X-ray imaging which shows a complex gas structure in the center of Mrk 6, are consistent with the idea of a jet that is changing its direction of propagation and interacting with the surrounding medium.

(ix) We find a continuum of radio properties between a subset of radio-loud Seyfert and FRI radio galaxies.

REFERENCES

Anderson J. M., Ulvestad J. S., 2005, ApJ, 627, 674

Balmaverde B., Capetti A., 2006, A&A, 447, 97

Bardeen J. M., Petterson J. A., 1975, ApJ, 195, L65

Baum S. A., O'Dea C. P., Dallacassa D., de Bruyn A. G., Pedlar A., 1993, ApJ, 419, 553

Beasley A. J., Conway J. E., 1995, in Astronomical Society of the Pacific Conference Series, Vol. 82, Very Long Baseline Interferometry and the VLBA, J. A. Zensus, P. J. Diamond, & P. J. Napier, ed., p. 328

Bicknell G. V., Dopita M. A., Tsvetanov Z. I., Sutherland R. S., 1998, ApJ, 495, 680

Bîrzan L., McNamara B. R., Carilli C. L., Nulsen P. E. J., Wise M. W., 2007, in Heating versus Cooling in Galaxies and Clusters of Galaxies, Böhringer H., Pratt G. W., Finoguenov A., Schuecker P., eds., p. 115

Bontempi P., Giroletti M., Panessa F., Orienti M., Doi A., 2012, MNRAS, 426, 588

Brunthaler A., Falcke H., Bower G. C., Aller M. F., Aller H. D., Teräsranta H., 2005, A&A, 435, 497

Buchanan C. L., Gallimore J. F., O'Dea C. P., Baum S. A., Axon D. J., Robinson A., Elitzur M., Elvis M., 2006, AJ, 132, 401

Burbidge G. R., 1959, ApJ, 129, 849

Capetti A., Axon D. J., Kukula M., Macchetto F., Pedlar A., Sparks W. B., Boksenberg A., 1995, ApJ, 454, L85

Chiaberge M., Capetti A., Celotti A., 1999, A&A, 349, 77

Colbert E. J. M., Baum S. A., Gallimore J. F., O'Dea C. P., Christensen J. A., 1996, ApJ, 467, 551

Doroshenko V. T., Sergeev S. G., Klimanov S. A., Pronik V. I., Efimov Y. S., 2012, MNRAS, 426, 416

Elmouttie M., Haynes R. F., Jones K. L., Sadler E. M., Ehle M., 1998, MNRAS, 297, 1202

Falle S. A. E. G., 1991, MNRAS, 250, 581

Fanaroff B. L., Riley J. M., 1974, MNRAS, 167, 31P

Gallimore J. F., Axon D. J., O'Dea C. P., Baum S. A., Pedlar A., 2006, AJ, 132, 546

Gallimore J. F. et al., 2010, ApJS, 187, 172

Gitti M., Giroletti M., Giovannini G., Feretti L., Liuzzo E., 2013, A&A, 557, L14

Gizani N. A. B., Leahy J. P., 2003, MNRAS, 342, 399

Gregory P. C., Condon J. J., 1991, ApJS, 75, 1011

Greisen E. W., 2003, in Astrophysics and Space Science Library, Vol. 285, Astrophysics and Space Science Library, A. Heck, ed., p. 109

Griffin M. J., Abergel A., Abreu A., 176 coauthors, 2010, A&A, 518, L3

Hardcastle M. J., Birkinshaw M., Worrall D. M., 1998, MNRAS, 294, 615

Hardcastle M. J., Ching J. H. Y., Virdee J. S., 25 coauthors, 2013, MNRAS, 429, 2407

Hardcastle M. J., Croston J. H., 2011, MNRAS, 415, 133

Hardee P. E., 1987, ApJ, 318, 78

Hjellming R. M., Johnston K. J., 1981, ApJ, 246, L141

Ho L. C., Peng C. Y., 2001, ApJ, 555, 650

Hota A., Saikia D. J., 2006, MNRAS, 371, 945

Kellermann K. I., Pauliny-Toth I. I. K., 1981, ARA&A, 19, 373

Kellermann K. I., Sramek R., Schmidt M., Shaffer D. B., Green R., 1989, AJ, 98, 1195

Kharb P. et al., 2012a, AJ

Kharb P., Hota A., Croston J. H., Hardcastle M. J., O'Dea C. P., Kraft R. P., Axon D. J., Robinson A., 2010, ApJ, 723, 580

Kharb P., O'Dea C. P., Baum S. A., Colbert E. J. M., Xu C., 2006, ApJ, 652, 177

Kharb P., O'Dea C. P., Baum S. A., Daly R. A., Mory M. P., Donahue M., Guerra E. J., 2008, ApJS, 174, 74

Kharb P., O'Dea C. P., Tilak A., Baum S. A., Haynes E., Noel-Storr J., Fallon C., Christiansen K., 2012b, ApJ, 754, 1

Kinney A. L., Schmitt H. R., Clarke C. J., Pringle J. E., Ulvestad J. S., Antonucci R. R. J., 2000, ApJ, 537, 152

Kukula M. J., Ghosh T., Pedlar A., Schilizzi R. T., 1999, ApJ, 518, 117

Kukula M. J., Holloway A. J., Pedlar A., Meaburn J., Lopez J. A., Axon D. J., Schilizzi R. T., Baum S. A., 1996, MNRAS, 280, 1283

Laing R. A., Bridle A. H., 2002, MNRAS, 336, 328

Li J., Jin W., 1996, A&AS, 120, 201

Ma C. et al., 1998, AJ, 116, 516

Mahadevan R., 1997, ApJ, 477, 585

Martí-Vidal I., Marcaide J. M., Alberdi A., Pérez-Torres M. A., Ros E., Guirado J. C., 2011, A&A, 533, A111

Merritt D., Ekers R. D., 2002, Science, 297, 1310

Middelberg E. et al., 2004, A&A, 417, 925

Miley G., 1980, ARA&A, 18, 165

Mingo B., Hardcastle M. J., Croston J. H., Evans D. A., Hota A., Kharb P., Kraft R. P., 2011, ApJ, 731, 21

Mingo B., Hardcastle M. J., Croston J. H., Evans D. A., Kharb P., Kraft R. P., Lenc E., 2012, ApJ, 758, 95

Nagar N. M., Falcke H., Wilson A. S., Ho L. C., 2000, ApJ, 542, 186

Napier P. J., 1994, in IAU Symposium, Vol. 158, Very High Angular Resolution Imaging, J. G. Robertson & W. J. Tango, ed., p. 117

Nixon C., King A., 2013, ApJ, 765, L7

O'Dea C. P., 1985, ApJ, 295, 80

O'Dea C. P., Baum S. A., Tremblay G. R., Kharb P., Cotton W., Perley R., 2013, ApJ, 771, 38

Orienti M., Prieto M. A., 2010, MNRAS, 401, 2599

Poglitsch A., Waelkens C., Geis N., 80 coauthors, 2010, A&A, 518, L2

Rees M. J., 1978, Nature, 275, 516

Rush B., Malkan M. A., Spinoglio L., 1993, ApJS, 89, 1

Schurch N. J., Griffiths R. E., Warwick R. S., 2006, MNRAS, 371, 211

Shulevski A., Morganti R., Oosterloo T., Struve C., 2012, A&A, 545, A91

Sikora M., Stawarz Ł., Lasota J.-P., 2007, ApJ, 658, 815

Stawarz Ł., Sikora M., Ostrowski M., 2003, ApJ, 597, 186

Terashima Y., Wilson A. S., 2003, ApJ, 583, 145

Ulvestad J. S., 2003, in Astronomical Society of the Pacific Conference Series, Vol. 300, Radio Astronomy at the Fringe, Zensus J. A., Cohen M. H., Ros E., eds., p. 97

Ulvestad J. S., Antonucci R. R. J., Barvainis R., 2005, ApJ, 621, 123

Ulvestad J. S., Ho L. C., 2001, ApJ, 562, L133

Urry C. M., Padovani P., 1995, PASP, 107, 803

van der Laan H., Perola G. C., 1969, A&A, 3, 468

Verdoes Kleijn G. A., Baum S. A., de Zeeuw P. T., O'Dea C. P., 1999, AJ, 118, 2592

Verdoes Kleijn G. A., Baum S. A., de Zeeuw P. T., O'Dea C. P., 2002, AJ, 123, 1334

Volonteri M., Sikora M., Lasota J.-P., 2007, ApJ, 667, 704

Wandel A., Peterson B. M., Malkan M. A., 1999, ApJ, 526, 579

Wilson A. S., Ulvestad J. S., 1982, ApJ, 263, 576
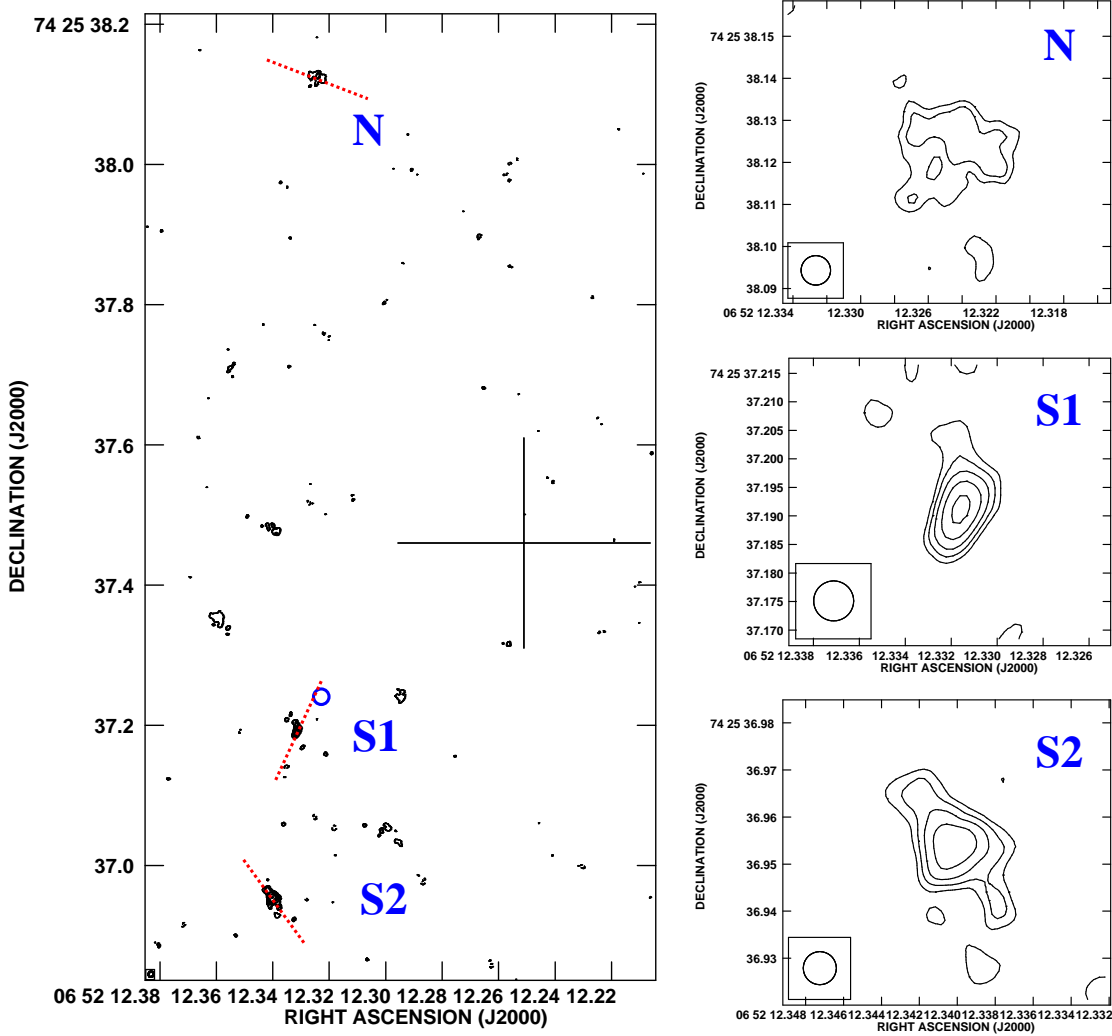
Woo J.-H., Urry C. M., 2002, ApJ, 579, 530

Figure 1. The 1.6 GHz radio image of Mrk 6: three components N, S1, and S2 are detected. The panels on the right show the zoomed-in images of the components. The red dashed lines indicate the PA of the component extensions. The contours for the right hand side panels are in percentage of peak intensity and increase in steps of $\sqrt{2}$. The peak intensity is 2.2 mJy beam^{-1}, and the lowest contour levels are for (N) $\pm 16\%$, (S1) $\pm 22.5\%$, and (S2) $\pm 22.5\%$. The images were convolved with circular beams of size 7 mas $\times$ 7 mas. The cross represents the centre of the optical host galaxy of Mrk 6 along with the uncertainty, while the small blue circle represents the position of the radio core seen only at 4.9 GHz.
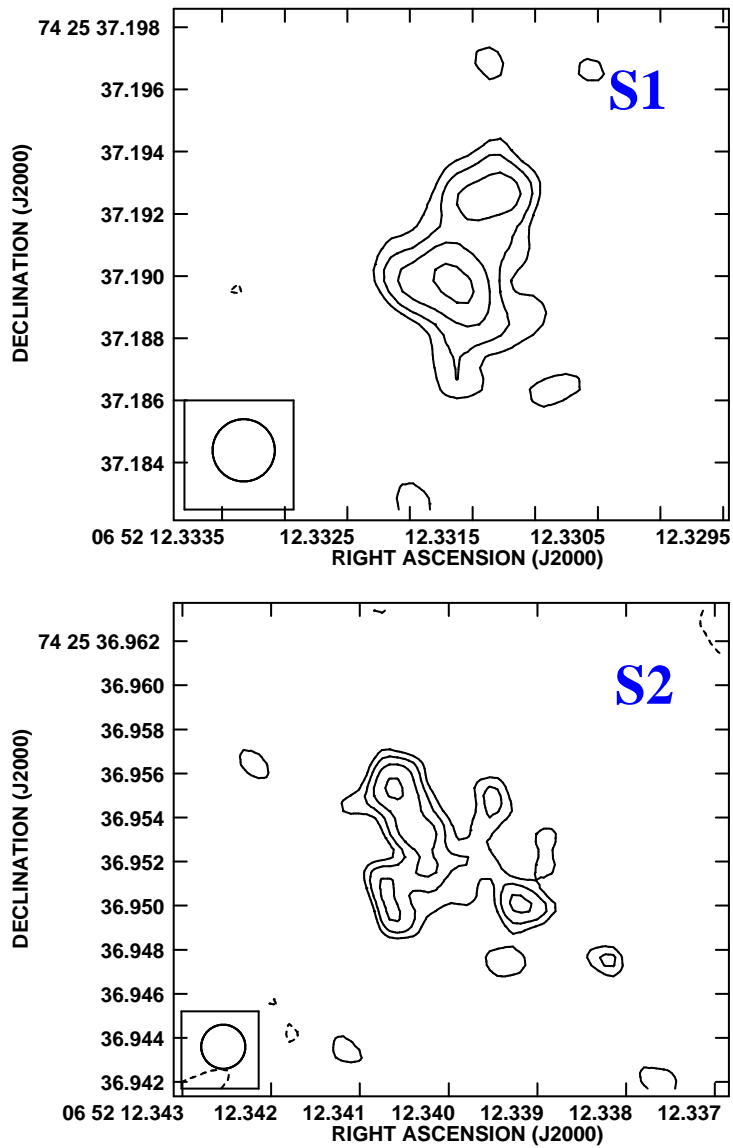
Figure 2. The 4.9 GHz radio image of Mrk 6: only components S1 (top) and S2 (bottom) are detected. Component S1 seems to have two peaks, although there seems to be more sub-structure. The contours are in percentage of peak intensity and increase in steps of $\sqrt{2}$. The peak intensity is 0.7 mJy beam^{-1}, and the lowest contour levels are for (S1) $\pm 32\%$ and (S2) $\pm 22.5\%$. The images were convolved with circular beams of size 2 mas $\times$ 2 mas.
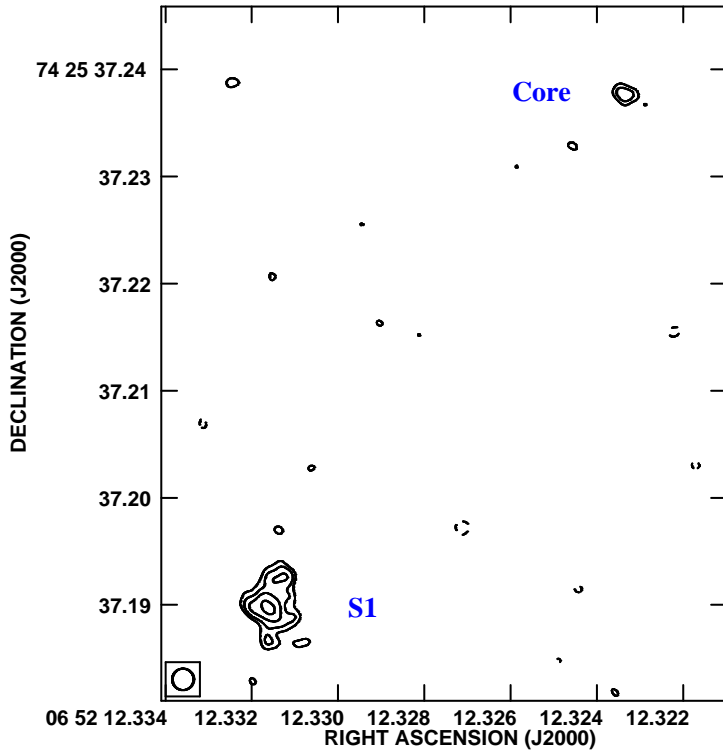
Figure 3. The 4.9 GHz radio image of Mrk 6 showing the radio core. The image is convolved with a circular beam of size 2 mas $\times$ 2 mas. The contours are in percentage of peak intensity and increase in steps of $\sqrt{2}$. The peak intensity is 0.7 mJy beam^{-1}, and the lowest contour levels are $\pm 32\%$. The distance between the core and component S1 is $0\rlap{.}{''}058$ or ≈ 22 pc.
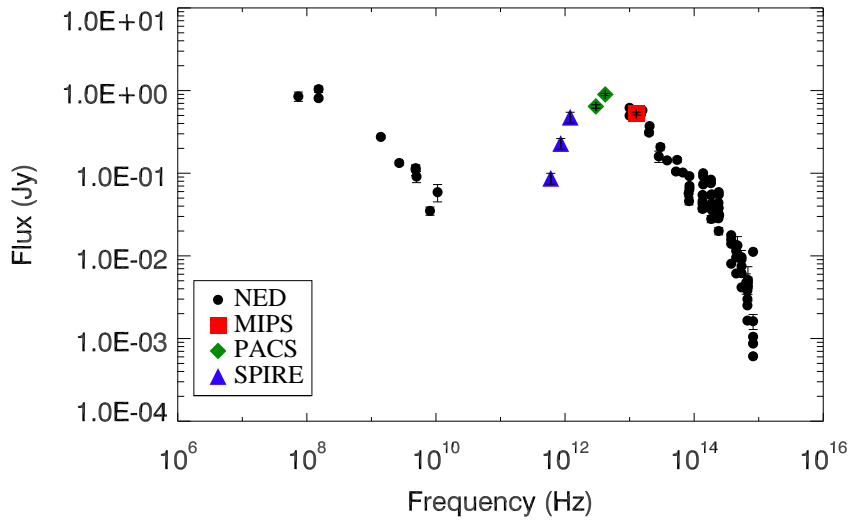
Figure 4. Broad-band SED of Mrk 6 with new infrared data from the *Herschel* space telescope. Other data are from NED.
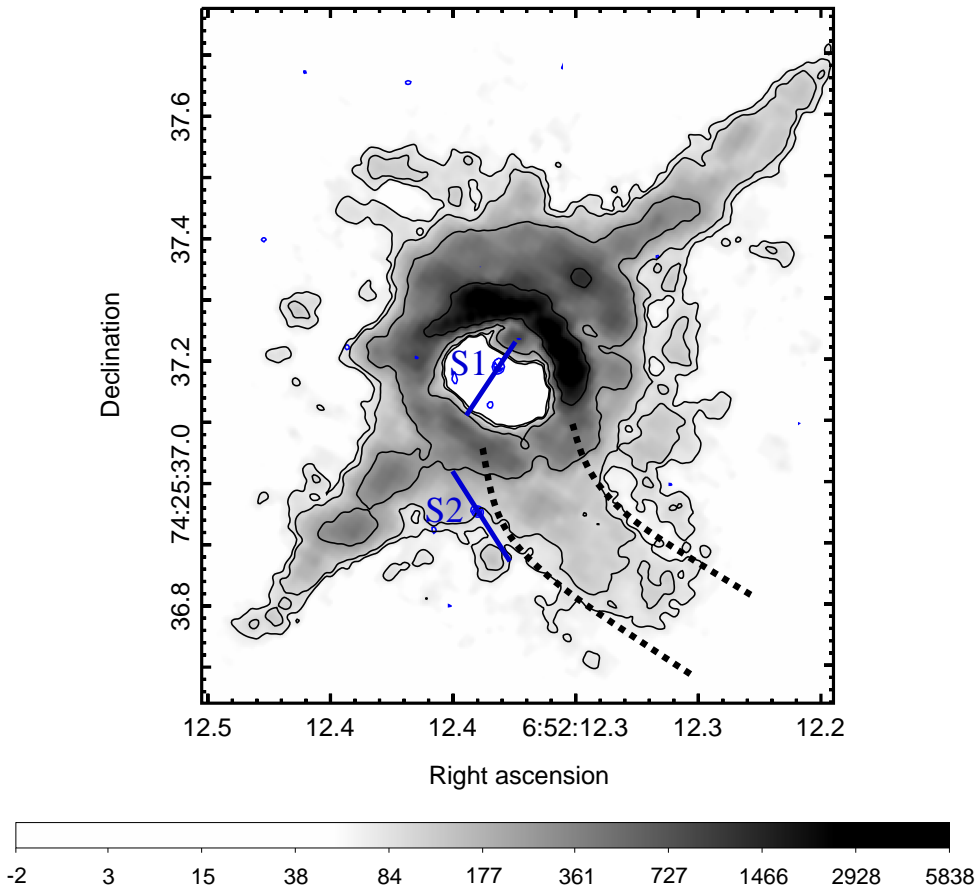
Figure 5. The *HST* archival FOC/F372M image showing the emission line gas structure highlighted by the black dashed lines in Mrk 6. The blue contours denote the VLBA emission. The PA of components S1 and S2 are represented by blue solid lines. Component S2 seems to lie at the outer edge of the curved emission line structure.
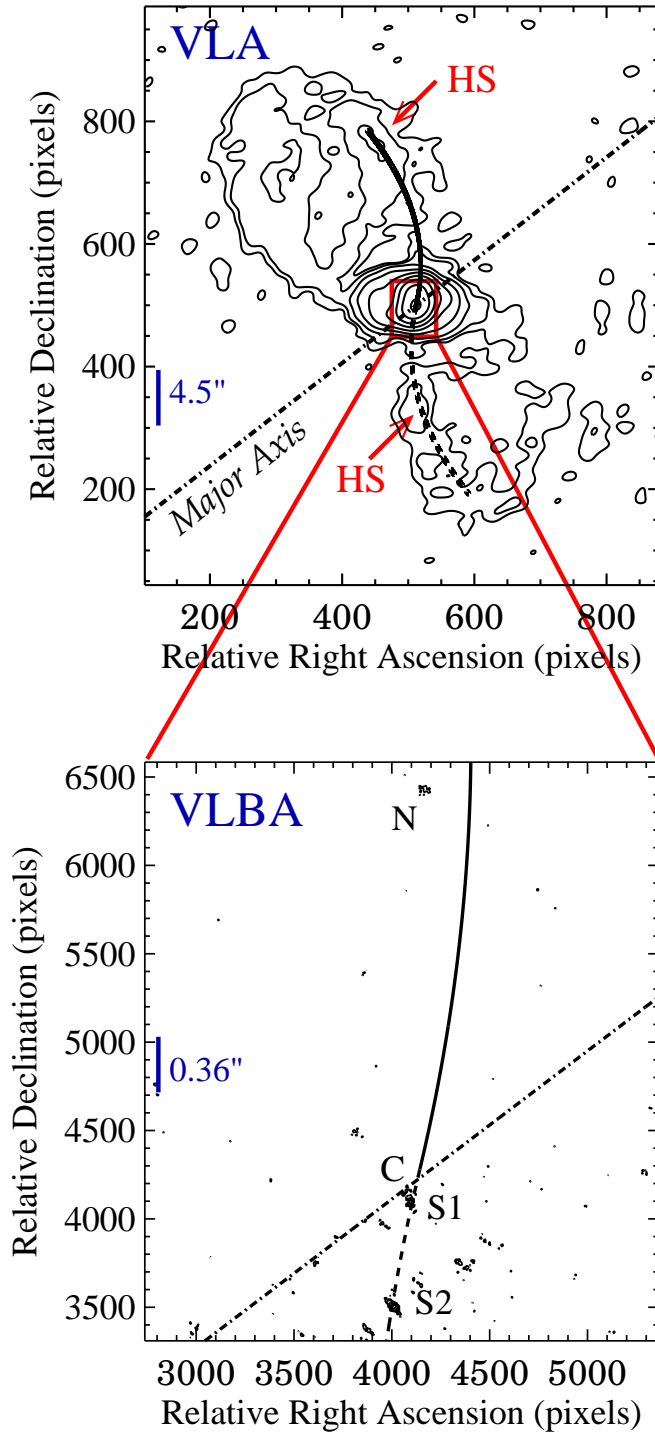
Figure 6. A precessing jet model shown in solid (representing jet) and dashed (representing counter-jet) lines connects the VLBA components (bottom panel, 1 pixel = 1.2 mas) to the hot spots, HS, in the VLA image (top panel, 1 pixel = 45 mas) of Mrk 6. The 20cm VLA image is reproduced from Kharb et al. (2006). The dot-dashed line indicates the major axis of the host galaxy bulge. The best fit model parameters are discussed in Section 4.2
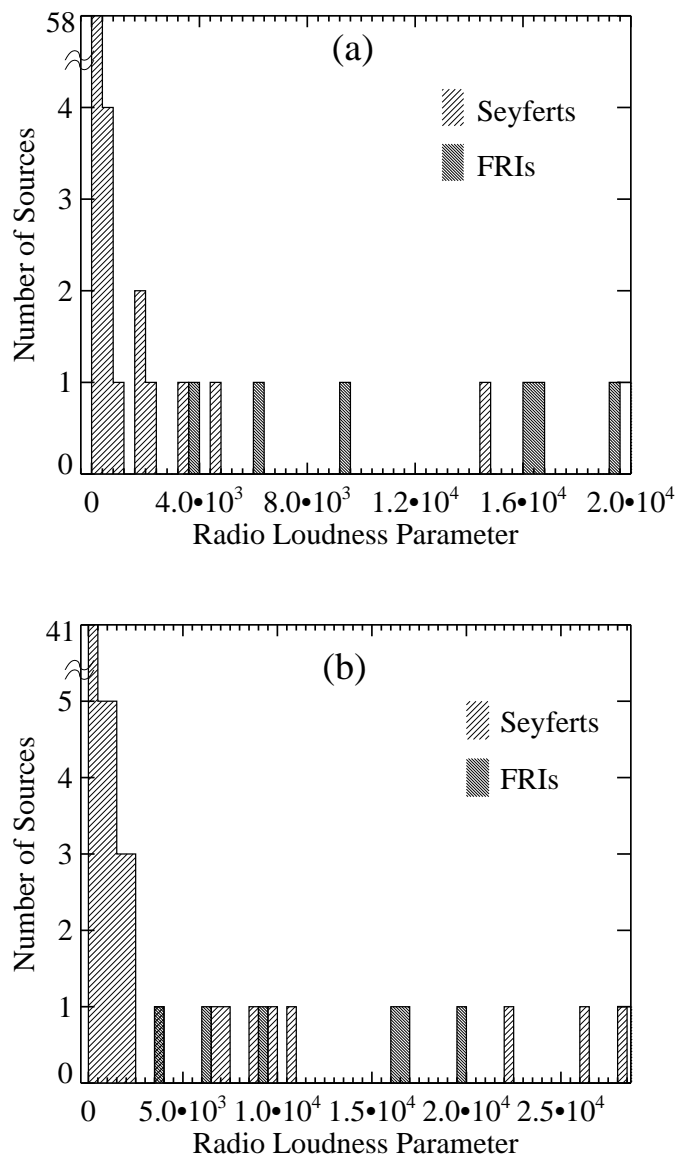
Figure 7. The radio-loudness parameter (R) for Seyfert galaxies belonging to the Extended 12μm sample (Rush, Malkan & Spinoglio 1993) and FRI radio galaxies belonging to the UGC sample (Verdoes Kleijn et al. 1999). For the estimation of R for the Seyfert galaxies, median nuclear absolute B-band magnitudes of the CfA (=−17.4) and the Palomar Seyfert samples (=−14.6; Ho & Peng 2001) were chosen for panels "a" (top) and "b" (bottom), respectively.

Figure 8. UGC03695: the FRI radio galaxy with the lowest radio loudness parameter in the sample under study. The black and white contours indicate the 1.4 GHz emission (levels are in percentage of peak intensity and increase in steps of 2; the lowest contour is at ± 0.17 percent of peak intensity = 128 mJy beam^{-1}), while the magenta contours indicate the 4.9 GHz emission (the lowest contour is at ± 0.3 percent of peak intensity = 99 mJy beam^{-1}; Noel-Storr et al., in preparation).

APPENDIX A: RADIO LOUDNESS OF A SELECTED SAMPLE OF FRI AND SEYFERT GALAXIES

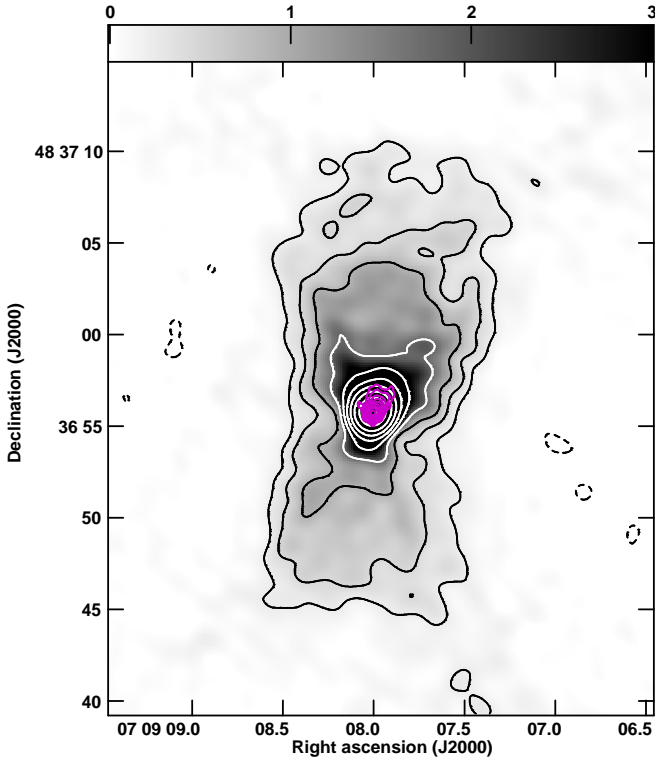We present the radio loudness parameters of a set of FRI radio galaxies belonging to the UGC sample (Verdoes Kleijn et al. 1999) and Seyfert galaxies belonging to the extended 12μm sample (Rush, Malkan & Spinoglio 1993), having taken into account their nuclear optical luminosities, in Table A1. We obtained the nuclear optical luminosities of the FRI radio galaxies from the F555W and F547W *HST* observations of Verdoes Kleijn et al. (2002). These were converted to B-band (4400Å) flux densities using an optical spectral index of -0.9 (e.g., Chiaberge, Capetti & Celotti 1999). A few FRI radio galaxies did not have *HST* data: total B-band magnitudes were used in their R estimation instead. These have an asterisk next to their R values. As most of the Seyfert galaxies considered here did not have *HST* data, we adopted the median nuclear absolute B-band magnitudes derived by Ho & Peng (2001). Two sets of radio loudness parameters were derived using the median nuclear absolute magnitudes for the CfA ($M_B^{nuc} = -17.4$) and Palomar ($M_B^{nuc} = -14.6$) Seyfert samples, respectively. After deriving the apparent nuclear magnitudes (m_B^{nuc}) for the sources at different redshifts, the optical nuclear flux density at 4400Å (S_o) was estimated using the relation: $S_o = 10^{((-m_B^{nuc}-48.36)/2.5)}$. The apparent B-band magnitudes and 5 GHz (=6cm) flux densities listed in Table A1 were obtained from NED. We note that with the exception of a few FRI radio galaxies (the ones with an asterisk next to their R values), these B-band magnitudes were not used in

the actual estimation of R for most sources, and are presented here for completeness.

We find that 66 percent of Seyfert 1s and 76 percent of Seyfert 2s are radio-loud taking into account the median nuclear magnitude of the CfA sample, while 89 percent of Seyfert 1s and 94 percent of Seyfert 2s are radio-loud taking into account the median nuclear magnitude of the Palomar sample. 17 Seyfert galaxies are common between the sample considered here and that for which nuclear R values were estimated by Ho & Peng (2001). The R values of nearly 76 percent of the common sources (i.e., 13 of 17 sources) lie in the range that we have derived in Table A1. The lower range of R values derived here are 50 and 100 times higher than those obtained by Ho & Peng for IZW1 and MK231, respectively, while the R values derived by Ho & Peng are 130 and 220 times higher than the upper range of R values derived here for N2639 and N3031, respectively. This gives us confidence that the range of R values derived for Seyfert galaxies here are truly representative of the sample.

Table A1. Radio Loudness Parameters

Source name	B-band mag	Flux@6cm mJy	R	Type
U00408	13.87	864.0	263788	FRI
U00597	12.23	1192.0	68375	FRI
U00689	13.38	2080.0	164054	FRI
U01004	13.49	77.6	19586	FRI
U01413	12.35	305.0	151932	FRI
U01841	13.75	2942.0	107096	FRI
U03695	13.60	339.0	3775	FRI
U05073	14.05	138.0	16326	FRI
U06635	12.57	635.0	15*	FRI
U06723	13.52	1674.0	16678	FRI
U07115	14.33	169.0	9409	FRI
U07360	11.37	4089.0	2.0E+06	FRI
U07455	13.40	82.0	6209	FRI
U07494	10.29	3582.0	109362	FRI
U07654	9.65	59740.0	176693	FRI
U08419	12.90	449.0	14*	FRI
U08433	13.79	421.0	83886	FRI
U09058	12.80	325.0	918210	FRI
U11718	13.40	122.0	6*	FRI
U12064	14.49	1146.0	158*	FRI
U12531	12.41	152.0	77764	FRI
MK335	14.13	3.6	11, 141	SY1
IZW1	14.59	3.1	51, 670	SY1
M-3-7-11	13.94	31.5	163, 2149	SY1
N931	13.90	1.7	2, 28	SY1
N1365	10.23	230.0	30, 393	SY1
N1566	10.13	100.0	11, 144	SY1
MK618	16.59	5.0	29, 380	SY1
MK6	14.80	115.0	181, 2382	SY1
MK9	15.20	1.8	13, 173	SY1
MK79	13.30	10.0	22, 290	SY1
N2639	12.40	119.2	65, 855	SY1
MK704	15.20	4.0	15, 204	SY1
U5101	15.50	79.0	562, 7405	SY1
N2992	12.63	102.0	27, 350	SY1
MK1239	14.50	32.0	56, 744	SY1
N3031	8.10	385.0	0.02, 0.28	SY1
N3227	12.20	35.0	2, 30	SY1
N3516	12.30	10.6	4, 48	SY1
N4051	11.50	32.0	1, 10	SY1
N4151	11.20	152.0	7, 96	SY1
MK766	13.70	15.8	12, 153	SY1
N4579	11.50	99.0	11, 145	SY1
N4593	11.67	3.8	1, 18	SY1

Table A1 – *continued*

Source name	B-band mag	Flux@6cm mJy	R	Type
N4594	8.56	156.0	8, 110	SY1
N4602	12.31	1.3	0.4, 5	SY1
M-2-33-34	17.50	6.0	5, 66	SY1
MK231	14.10	419.0	3433, 45258	SY1
N5033	10.90	82.0	3, 40	SY1
M-6-30-15	13.86	1.0	0.3, 4	SY1
N5548	13.10	13.8	18, 238	SY1
MK817	14.30	6.0	27, 355	SY1
MK509	11.83	5.5	29, 388	SY1
N7213	11.49	249.0	37, 488	SY1
N7469	13.00	95.0	112, 1478	SY1
N7603	14.40	20.0	79, 1039	SY1
N7674	13.52	86.0	2141, 28223	SY2
N7582	11.26	143.0	61, 807	SY2
I5063	12.86	524.0	4757, 62709	SY2
N6810	12.36	72.0	14, 190	SY2
U9913	13.90	208.0	746, 9829	SY2
N5953	13.30	40.0	26, 346	SY2
N5929	12.99	42.0	35, 463	SY2
N5506	13.60	227.2	92, 1219	SY2
MK463	14.80	118.0	14473, 190789	SY2
N5347	13.30	3.1	3, 36	SY2
MK273	15.00	103.0	1677, 22107	SY2
N5256	14.10	49.0	818, 10781	SY2
N5194	8.80	1135.0	22, 295	SY2
N5135	12.76	107.0	291, 3835	SY2
N5005	10.60	72.0	22, 284	SY2
N4941	12.10	9.0	0.5, 7	SY2
N4501	10.60	102.4	189, 2498	SY2
N4388	12.20	93.0	54, 709	SY2
N3982	11.60	24.0	8, 104	SY2
N3660	12.69	0.8	0.5, 7	SY2
N3079	11.20	327.0	122, 1604	SY2
N1667	13.12	45.0	135, 1780	SY2
N1386	12.24	13.0	3, 45	SY2
N1320	13.32	3.3	5, 61	SY2
N1241	12.64	12.3	10, 129	SY2
N1194	14.70	1.5	3, 45	SY2
N1097	9.96	150.0	90, 1182	SY2
N1068	9.70	2187.0	672, 8858	SY2
N1056	13.50	4.8	34, 442	SY2
F01475-0740	17.13	278.0	502, 6624	SY2
N513	13.40	57.0	83, 1100	SY2
N262	15.00	681.0	125, 1649	SY2

Column 1 lists the names of FRI radio galaxies from the UGC sample (Verdoes Kleijn et al. 1999) and Seyfert galaxies from the Extended 12μm sample (Rush, Malkan & Spinoglio 1993), that were used for the current study. Columns 2 and 3 list their apparent B-band magnitudes and 5 GHz (=6cm) flux densities, respectively. These were obtained from NED. The nuclear optical luminosities for the FRI radio galaxies were obtained from the *HST* data of Verdoes Kleijn et al. (2002). Column 4 lists the radio-loudness parameters, R. $*$ denotes those FRIs for which *HST* data were unavailable − for these the B-band magnitudes listed here were used instead. As most Seyferts did not have *HST* data, two median nuclear absolute magnitudes of the CfA (=−17.4) and Palomar Seyfert samples (=−14.6; Ho & Peng 2001) were chosen, to derive two sets of R values. (Note: The B-band magnitudes listed here were not used in the estimation of R for the Seyfert and most of the FRI galaxies.)